CrossMark

ORIGINAL ARTICLE

Effect of heat input on microstructure and mechanical properties of pulsed laser welded joints in Ti6Al4V/Nb dissimilar alloys

Xiao-Long Gao[1] · Jing Liu[1] · Lin-Jie Zhang[2]

© Springer-Verlag London Ltd. 2017

Abstract Pulsed laser welding was used to weld dissimilar joints in Ti6Al4V/Nb alloys. The effect of heat input on the microstructural characterizations and mechanical properties of the joints was investigated. The experimental results show that underfill defects disappeared in the fusion zone (FZ) as the heat input increased. No intermetallic compounds were formed in the FZ, but a dendritic zone of Ti-rich phases and an island zone of Nb-rich phases were present for all welded joints, indicating that composition segregation occurred in the Ti6Al4V/Nb dissimilar joint. Moreover, the microstructure and mechanical heterogeneity in the FZ of the welded joint increased with increasing heat input. The microhardness of the island area was lower than that of the dendritic zone in the FZ, because it possessed higher levels of Nb. The results of the tensile tests show that the joints fractured at the Nb base metal side, suggesting that the strength of the FZ is higher than that of the Nb base metal.

1 Introduction

Ti6Al4V has extensive application in the aerospace, automotive, petrochemical, nuclear, and medical industries, because it

✉ Xiao-Long Gao
gaoxiaolong503@163.com

1 School of Mechanical Engineering, Baoji University of Arts and Sciences, Baoji 721016, China

2 State key laboratory of mechanical behavior for materials, Xi'an Jiaotong University, Xi'an 710049, China

possesses good corrosion resistance, high strength, and creep resistance [1, 2]. Niobium is a refractory metal with many desirable properties such as superior superconducting properties and high electrical and thermal conductivity [3]. Niobium to Ti6Al4V dissimilar joints have been used in the fabrication of superconducting radio frequency (SRF) cavities, which are widely used for particle accelerators in many physics laboratories worldwide [4].

Dissimilar material welding has consistently drawn attention in industry, because it can effectively reduce material costs and weight, increase design flexibility and complexity, and improve product functionality [5, 6]. However, directly joining dissimilar materials can cause serious problems if the physical and chemical properties of the constituent metals differ considerably, resulting in degradation of mechanical properties of the weld. Chen et al. investigated welding cracks in direct laser welded NiTiNb shape memory alloys to Ti6Al4V alloys and found that the number of cracks and the cracking width first increased and then decreased with increasing laser power [7]. Miranda et al. demonstrated that laser welding of Ti6Al4V and NiTi is difficult due to the formation of intermetallic compounds, and filler materials or interlayers are needed to prevent the formation of brittle intermetallic phases [8]. Satoh et al. butt-welded titanium (Ti) to SS316 using pulsed laser welding to investigate the solidified microstructure. They found that an asymmetric shape of the weld and brittle Fe-Ti intermetallic compounds were readily generated within the weld with macroscopic cracks [9].

In dissimilar metal welding, interlayers with a melting point higher than the two base materials can prevent mixture of the two base metals in the molten pool [10, 11]. The melting point of niobium is significantly higher than that of most other metals; thus, it is identified as a potential interlayer for joining Ti6Al4V with other metals. Kundu et al. have found that Nb is an excellent diffusion

🍎 Springer

Table 1 Chemical compositions of the Ti6A4V titanium alloy and Nb (wt%)

	Ti	Al	V	Nb	Fe	Ta	N	H	O
Ti6Al4V	Balance	5.5–6.8	3.5–4.5	–	< 0.3	–	< 0.04	< 0.015	< 0.15
Nb	–	–	–	Balance	< 0.005	< 0.1	< 0.015	< 0.001	< 0.015

barrier between Ti and stainless steel in dissimilar welding [12]. Zhang et al. demonstrated that no Ti-Fe intermetallic species were detected in the weld during the pulsed laser welding of the Ti6Al4V alloy to SUS301L stainless steel with a Nb sheet as the interlayer [13]; in this case, diffusion and reaction between Ti and Fe was effectively prevented. Therefore, investigating the welding behavior of Nb with Ti is very important for reducing the formation of intermetallic phases and overcoming the physical and thermal property differences between dissimilar metals.

Compared with other welding processes, pulsed laser welding is the most suitable approach for welding dissimilar materials, because it allows more precise heat input control and high accuracy of the energy input position [14]. By judicious choice of the design variables, including pulse shaping, pulse energy, pulse duration, pulse repetition rate, and peak power, the incident laser energy and the heating/cooling rates inside the melting pools can be controlled [15]. Chen et al. examined the effect of pulse profiles on the performance of laser-welded CP Ti to stainless steel dissimilar joints; they found that stronger welds with superior homogeneity and a complex fracture mode were achieved when a ramp-down pulse profile was used compared with the use of a normal rectangular pulse profile [16]. When Nb was used as the interlayer to join NiTi and Ti6Al4V, Oliveira et al. found that optimal results were achieved when the pulse laser was focused near the Ti6Al4V-Nb interface. Ti6Al4V and the Nb sheet partially melted, and fusion welding occurred at the Ti6Al4V-Nb interface; a eutectic reaction was responsible for joining the NiTi-Nb interface [17].

However, dissimilar metals within the molten pool did not mix completely during the pulsed laser welding due to the high thermal gradients and short thermal cycle. Islands of Ti-rich and Nb-rich phases in the fusion zone (FZ) for laser-welded pure niobium- and Ti6Al4V-welded joints were observed by Torkamany et al., indicating a lack of mixing of the two materials in the pool [18]. Moreover, their experimental results demonstrated that a higher degree of penetration into niobium was obtained when Ti6Al4V absorbed the laser energy, which led to the dissolution of the niobium metal by the molten Ti6Al4V [19, 20]. However, the effect of welding parameters on the weld morphology, the dilution and homogeneity of the chemical composition in the FZ, as well as the microstructure and mechanical property of pulsed fiber laser-welded pure niobium to Ti6Al4V with full penetration has not yet been reported.

To this end, this work examines the butt-welding of pure niobium to Ti6Al4V alloy using a pulsed fiber laser. The effect of heat input on the weld quality of dissimilar materials with different thermo-physical properties is investigated.

2 Experimental materials and methods

Annealed sheets (100 mm × 50 mm, 0.8 mm thickness) of Ti6Al4V and Nb were autogenously laser beam welded using an IPG YLS-4000 multi-mode fiber laser system. This welding equipment has a maximum output of 4 kW and a transmission fiber diameter of 0.2 mm, and the focusing lens diameter and focal length are 50 and 150 mm, respectively. The chemical compositions and microstructure of Ti6Al4V and the niobium base metal are shown in Table 1 and Fig. 1, respectively. An optical microstructure image of the Ti6Al4V alloy is depicted in Fig. 1a, which is composed of equiaxed α phase and

Fig. 1 Microstructure of the base metals. **a** Ti6Al4V and **b** niobium
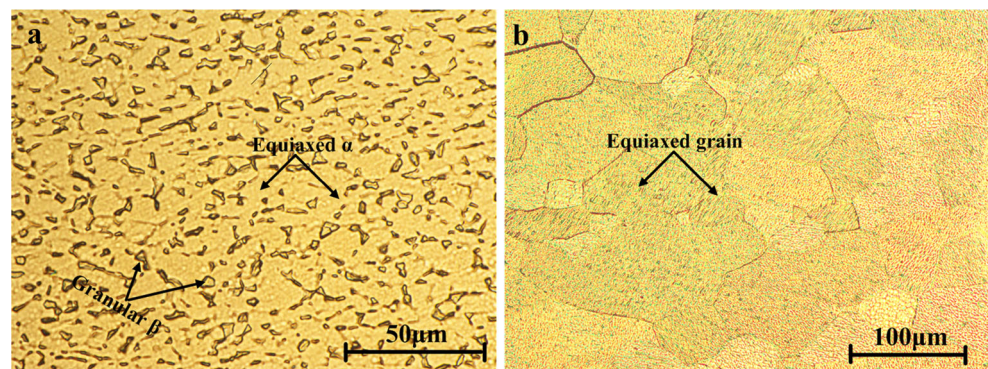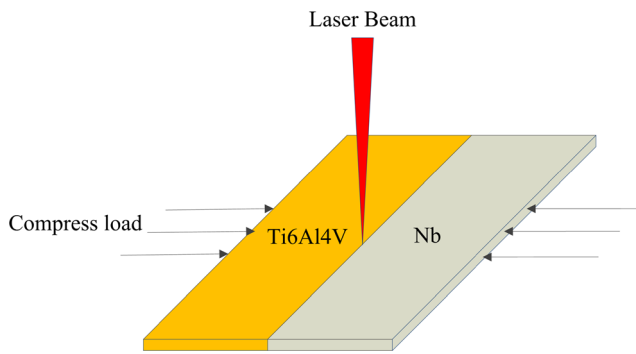
Fig. 2 Diagram of the laser welding process

Fig. 3 Schematic of the shielding gas device

granular β phase microstructures. The microstructure of the niobium alloy consists of equiaxed grains, as shown in Fig. 1b.

A diagram of the pulsed laser welding process and its associated welding parameters are presented in Fig. 2 and Table 2, respectively. To obtain a good weld, cleaning the materials before welding and using a shielding gas are necessary during the welding process. The plates were mechanically wire brushed, acid pickled in a HF solution, and then cleaned with acetone prior to welding. In the experiments, argon was used as the shielding gas to protect the FZ zone and the heat-affected zone (HAZ) from air contamination. Figure 3 shows that the side-blowing and back-shielding gas flows were delivered to the high-temperature zone at flow rates of 25 and 17 L min^{-1}, respectively.

After welding, the welds were sectioned transverse to the welding direction, mounted in a resin, and polished mechanically. Since the weld was composed of two different materials, a tailored two-step procedure for chemical etching was designed. In the first step, the Ti6Al4V side and fusion zone were etched with 3 mL HF + 5 mL HNO$_3$ + 100 mL H$_2$O, and in the second step, the Nb side was etched with 10 mL HF + 20 mL HNO$_3$ + 10 mL H$_2$O. The macroscopic appearance and microstructure of the welds were characterized using optical microscopy (OM) and scanning electron microscopy (SEM). To study the effect of heat input on the dilution and homogeneity of the chemical composition in the FZ, energy dispersive spectrometry (EDS) was performed on the transverse sections of the joints. Vickers microhardness measurements were carried out on the transverse sections under a load

of 200 g with a dwelling time of 15 s. The dimensions of the tensile test specimens are given in Fig. 4. Tensile testing was carried out at room temperature on a universal tensile test system with a constant drawing speed of 2 mm min^{-1}.

3 Results and discussion

The heat input depends on the peak power, pulse duration, pulse frequency, welding speed, and welding efficiency during pulsed laser welding. The heat input (E) can be calculated as shown in Eq. [1]:

$$E = \frac{P \times t \times f}{v} \times \eta \qquad (1)$$

where E is the heat input (J mm^{-1}), P is the peak power (kW), t is the pulse duration (ms), f is the pulse frequency (Hz), v is the welding speed (mm s^{-1}), and η is the welding efficiency.

As the efficiency does not change for the same material and welding process, η can be assumed as a constant value of approximately 1. It is evident that the weld heat input increases with increasing pulse duration for fixed values of peak power, pulse frequency, and welding speed. The welding heat input values used in this work are given in Table 2.
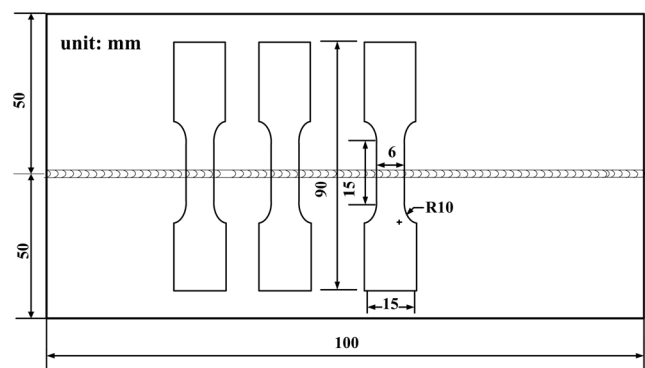
Table 2 Welding parameters of laser beam welding

Peak power/ kW	Welding speed/ m min^{-1}	Pulse frequency/ Hz	Focal position/ mm	Pulse duration/ ms	Heat input/ J mm^{-1}
1.5	1	50	1	5, 10, 15	22.5, 45.0, 67.5

Fig. 4 Schematic representation of the tensile specimen extraction (all dimensions are in "mm")

Fig. 5 Welded surface
morphologies with different heat
inputs. **a** 22.5 J mm^{-1}, **b**
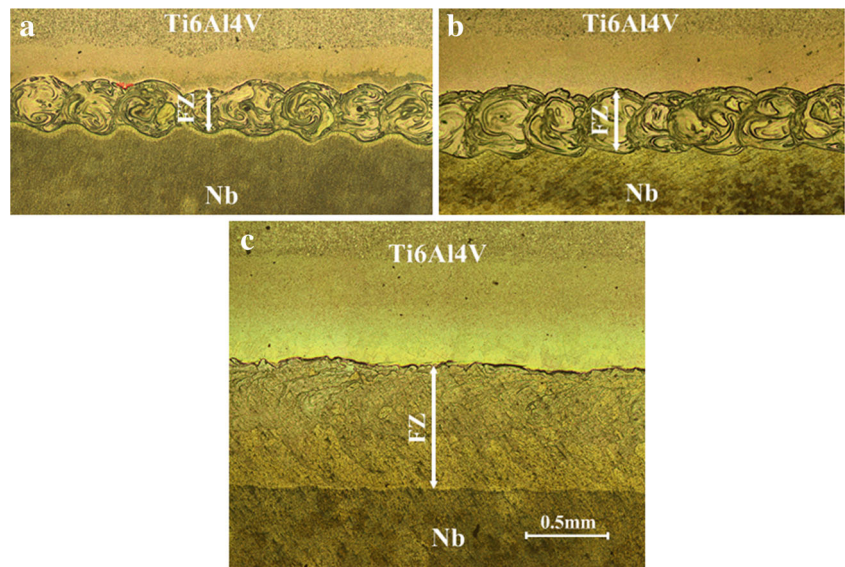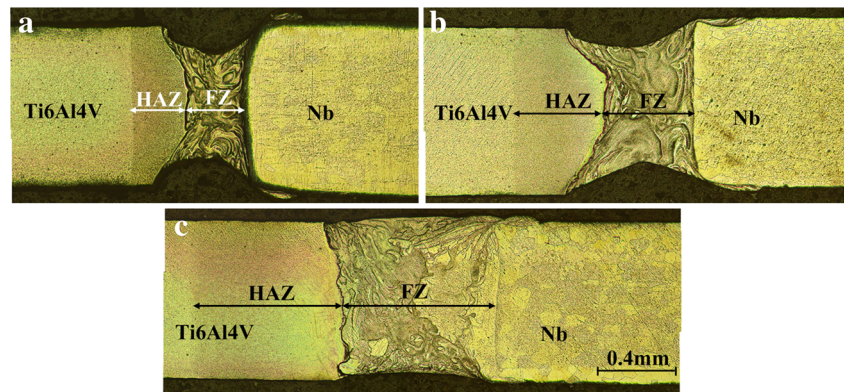45 J mm^{-1}, and **c** 67.5 J mm^{-1}

Fig. 6 Cross-sectional
morphologies of welded joints
with different heat inputs. **a**
22.5 J mm^{-1}, **b** 45 J mm^{-1}, and **c**
67.5 J mm^{-1}

3.1 Appearance of the weld joints

Figure 5 shows the top surface morphology of the laser-
welded Ti6Al4V/Nb dissimilar joints for different heat inputs.
When the heat input is low, the weld nugget boundaries are
especially clear and its shape is irregular, as shown in Fig. 5a,
b. When the heat input increases to 67.5 J mm^{-1}, the weld
nugget boundaries become difficult to distinguish, indicating
that the degree of overlap in the weld nugget increases with
increasing heat input. This is caused by the increase of the
melt pool volume at high heat input.

Figure 6 shows the cross sections of the laser-welded
Ti6Al4V/Nb dissimilar joints for different heat inputs. As
seen, the FZ width increased with increasing heat input.
Figure 6 also shows some typical defects apparent in the
welded joint. Underfill defects on the top and bottom of
the weld transverse sections are visible for the welded
joints with heat inputs of 22.5 and 45 J mm^{-1}, as shown
in Fig. 6a, b. However, underfill defects disappear when
the heat input is increased to 67.5 J mm^{-1}. The heat-

affected zone at the Nb side of the laser welded
Ti6Al4V/Nb dissimilar joint is difficult to distinguish,
whereas its width on the Ti6Al4V side can be clearly
observed. As the heat input is increased, the width of
the heat-affected zone on the Ti6Al4V side increases sig-
nificantly, which may be caused by the low phase transi-
tion temperature and thermal conductivity of Ti6Al4V.
Moreover, an interesting phenomenon concerning forma-
tion of the melt pool can be observed in the Ti6Al4V/Nb

Table 3 Comparison of thermo-physical properties of Ti6Al4V and
niobium alloys [18]

Material	Melting point (°C)	Boiling point (°C)	Density[a] (g cm^{-3})	Specific heat[a] C_p (J/(g·K))	Thermal conductivity[a] (W/(m·K))
Ti6Al4V	1655	3315	4.43	0.61	6.7
Nb	2468	4900	8.55	0.27	52

[a] Measured at 20 °C

Fig. 7 Microstructures of FZ in the joints welded with $E = 22.5$ J mm^{-1}
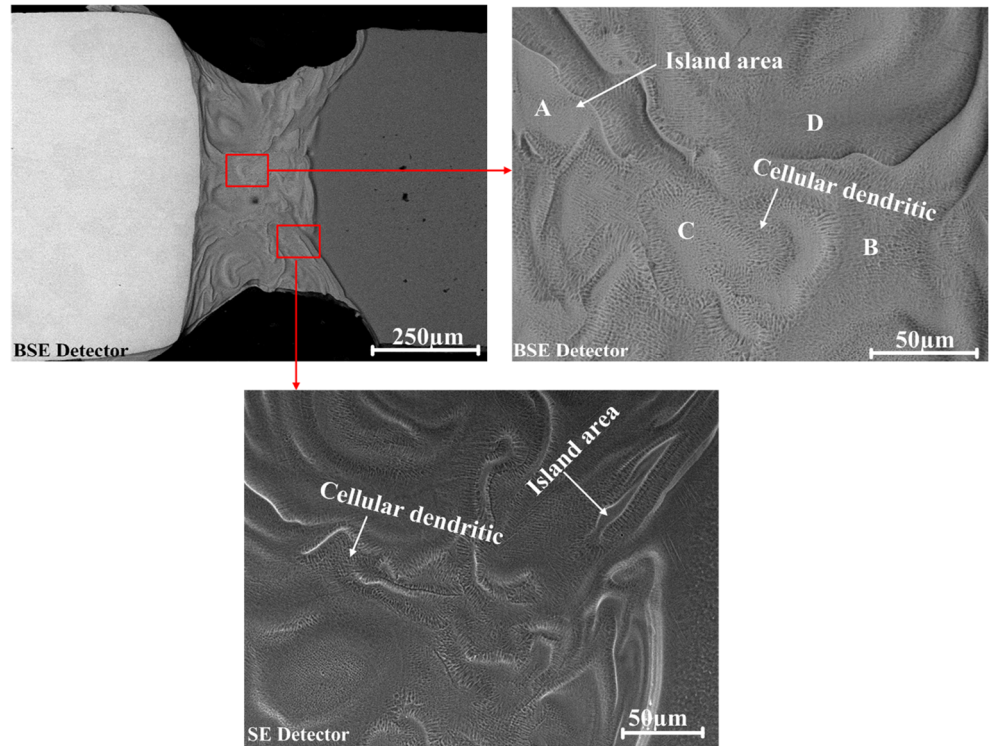
dissimilar joints. Specifically, the FZ/Ti6Al4V interface is tortuous, whereas the FZ/Nb interface is essentially straight. This result suggests that there is a tendency for the melt pool to be pulled irregularly into the Ti6Al4V side during laser welding of the Ti6Al4V/Nb dissimilar metals. As shown in Table 3, the melting point, boiling point, and thermal conductivity of Ti6Al4V are considerably lower than those of the Nb alloy. When the laser

Table 4 EDS analysis in the FZ of the joints welded with $E = 22.5$ J mm^{-1}

Atom percent/at.%	Ti	Al	V	Nb
A	63.64	11.56	2.33	22.47
B	77.21	10.48	3.09	9.22
C	79.08	10.43	2.85	7.64
D	64.40	11.50	2.46	21.64

beam was irradiated on the Ti6Al4V/Nb interface, the laser energy received by the Ti6Al4V side is more than that by the Nb side, resulting in asymmetric of the weld pool formed at the Ti6Al4V/Nb interface. A similar non-symmetrical weld pool has been reported by Torkamany et al. in the pulsed laser beam welding of Ti6AlV and a niobium alloy [18]. Even at relatively low magnification, it is also observed that the FZ microstructure for the welded joints with high heat input differs from the welded joints with low and medium heat inputs.
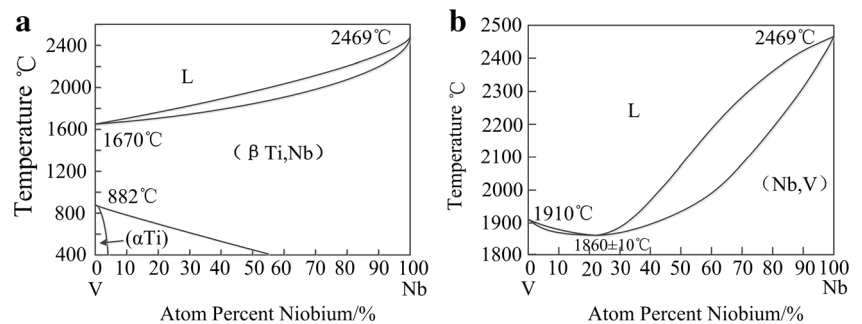
3.2 Microstructure of the fusion zone with different heat inputs

Figure 7 and Table 4 show the microstructure and corresponding EDS analysis in the FZ of the joints welded at $E = 22.5$ J mm^{-1}, respectively. The microstructure in the FZ is comprised of an island area and a dendritic zone;

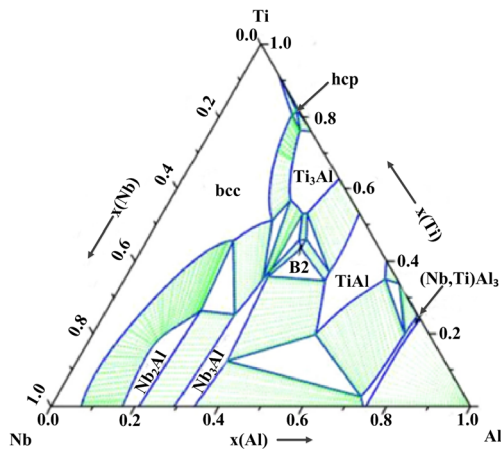**Fig. 8** Binary phase diagrams of **a** Ti/Nb and **b** Nb/V [20]

Fig. 9 Ternary Ti-Nb-Al phase diagram at 1150 °C [22]

Table 5 EDS analysis in the FZ of the joints welded with $E = 45$ J mm^{-1}

Atom percent/at.%	Ti	Al	V	Nb
A	73.64	10.87	2.27	13.22
B	64.38	7.89	2.07	25.66
C	65.74	8.63	2.34	23.30
D	73.51	9.87	2.90	13.72

the interface between these regions is obvious. According to the EDS analysis, the Nb content is higher in the island area than in the dendritic area, indicating that macrosegregation would occur in the Ti6Al4V/Nb dissimilar joint. Oliveira et al. discussed the mechanisms for the formation of island areas with macrosegregation features in the pulsed laser welding of super elastic NiTi and CuAlMn shape memory alloys [21]. The formation of island areas is related to the liquidus temperature of the weld metal, and to the base materials and fluid flow of the molten pool. Figure 8 shows a binary phase diagram of the Ti/Nb and Nb/V alloys. As can be seen, no intermetallic compounds can form in a Ti/Nb and Nb/V dissimilar

metal [22]. Figure 9 shows a ternary Al-Ti-Nb phase diagram, where the obtained phase is indicated [23]. According to this ternary phase diagram and the EDS analysis, formation of intermetallic compounds between niobium and aluminum in the melt pool is not plausible in Ti6Al4V/Nb dissimilar joints; thus, the formation of intermetallic species does not occur. According to the Ti/Nb binary phase diagram, the melting point of mixed (Ti, Nb) melted metal will increase as the Nb content increases. Accordingly, the melting point of the cellular dendritic structure is lower than that of the island area, suggesting that the island area solidified earlier than the cellular dendritic structure after the laser pulse ended.

Figure 10 and Table 5 show the microstructure and corresponding EDS analysis in the FZ of the joints welded at $E = 45$ J mm^{-1}, respectively. The microstructure in the FZ of these joints is very similar to the joints welded at $E = 22.5$ J mm^{-1}, except that the number of island areas in the FZ of the joints welded at $E = 45$ J mm^{-1} is smaller than

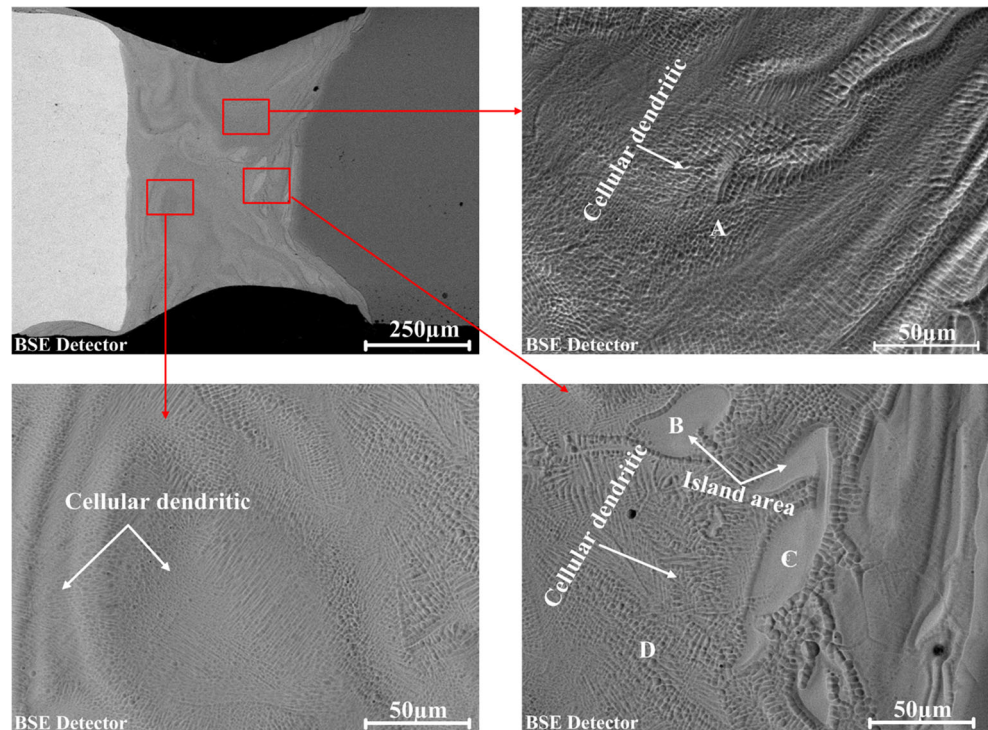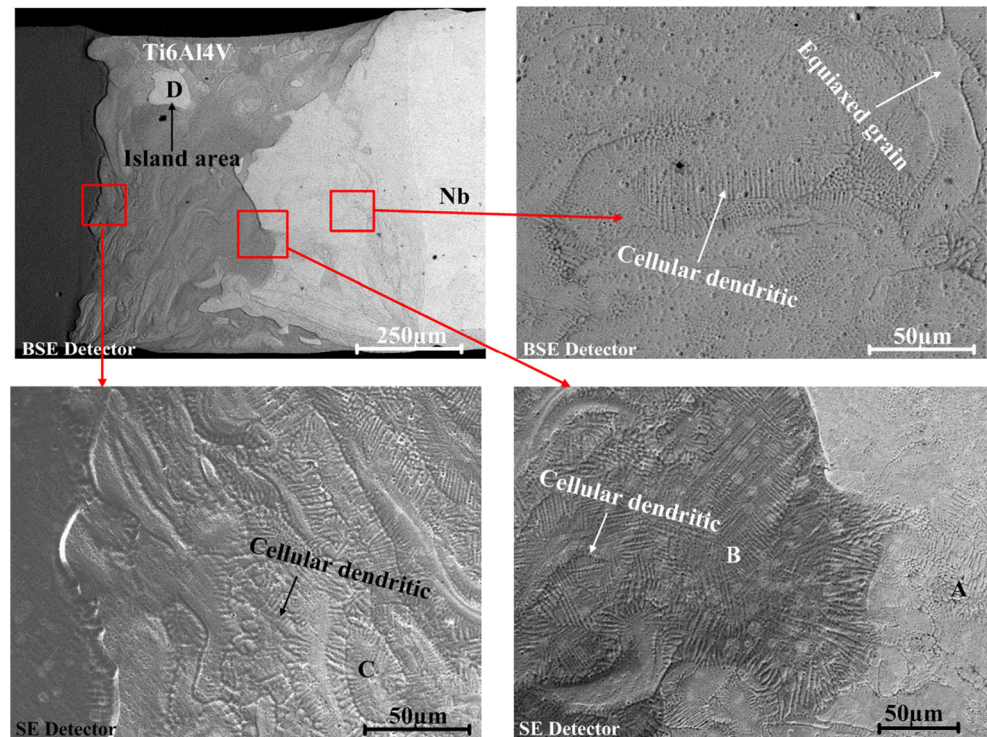Fig. 10 Microstructures of the FZ in the joints welded with $E = 45$ J mm^{-1}

Fig. 11 Microstructures of the FZ in the joints welded with $E = 67.5$ J mm^{-1}

that in the FZ of the joints welded at $E = 22.5$ J mm^{-1}. Tables 4 and 5 show that the Nb content in the dendritic zone in the $E = 45$ J mm^{-1} welded joint is higher than that in the $E = 22.5$ J mm^{-1} welded joint. Further, the difference in the Nb content between the island area and the cellular dendritic structure for the $E = 45$ J mm^{-1} welded joint decreased compared with the $E = 22.5$ J mm^{-1} welded joint. When both Ti6Al4V and pure Nb sheets were melted, the two materials mixed with each other within the melting pool. As the heat input increased, there was more time for the material to absorb laser energy through keyholes on the Nb side [19]. Compared with the joint welded at $E = 22.5$ J mm^{-1}, more Nb was melted and Ti and Nb within the melting pool had more time to mix for the welded joint at $E = 45$ J mm^{-1}, resulting in a decreased number of island areas and an increased Nb content in the FZ.

Figure 11 and Table 6 show the microstructure and corresponding EDS analysis in the FZ of the joints welded at $E = 67.5$ J mm^{-1}, respectively. The microstructural characteristics in the FZ of this welded joint differ from those at $E = 22.5$ J mm^{-1} and $E = 45$ J mm^{-1}. The microstructure in the FZ near the Ti6Al4V side is comprised of an island area and a dendritic zone, whereas the microstructure in the FZ near the Nb side is comprised of a cellular structure within an equiaxed crystal. As shown in Table 6, the Nb content (at.%) of the FZ at positions A and D is greater than 75%, whereas it is lower than 28% at positions B and C. According to the Ti/Nb binary phase diagram, the microstructure at positions A and D is solid solutions of (β Ti, Nb), whereas the microstructure at positions B and C is solid solutions of (α + β

Ti, Nb). When the heat input is less than 45 J mm^{-1}, the microstructure in the FZ for Ti6Al4V/Nb dissimilar joints only includes solid solutions of (α + β Ti, Nb).

Figures 12, 13, and 14 present the SEM-EDS linescanning results of the welded joints with heat inputs of 22.5, 45, and 67.5 J mm^{-1}, respectively. The distribution of Ti, Al, V, and Nb along the selected line in the FZ is heterogeneous, indicating a lack of Ti and Nb mixing within the melting pool. The difference in composition of dissimilar metals and the high heating and cooling rates of the pulsed laser welding process contributed to this lack of mixing. When the heat input is less than 45 J mm^{-1}, the Nb content is less than the Ti content in the molten pool. When heat input is 67.5 J mm^{-1}, however, the Nb content is less than the Ti content in the molten pool near the Ti6Al4V side, but the Nb content is larger than the Ti content in the molten pool near the Nb side. The elemental fluctuations of the welded joints

Table 6 EDS analysis in the FZ of the joints welded with $E = 67.5$ J mm^{-1}

Atom percent/at.%	Ti	Al	V	Nb
A	20.17	3.05	0.88	75.90
B	61.58	8.27	2.01	28.14
C	65.36	8.53	2.18	23.93
D	11.54	1.44	6.14	80.88

Fig. 12 SEM-EDS line-scanning results of the joints welded with $E = 22.5$ J mm^{-1}
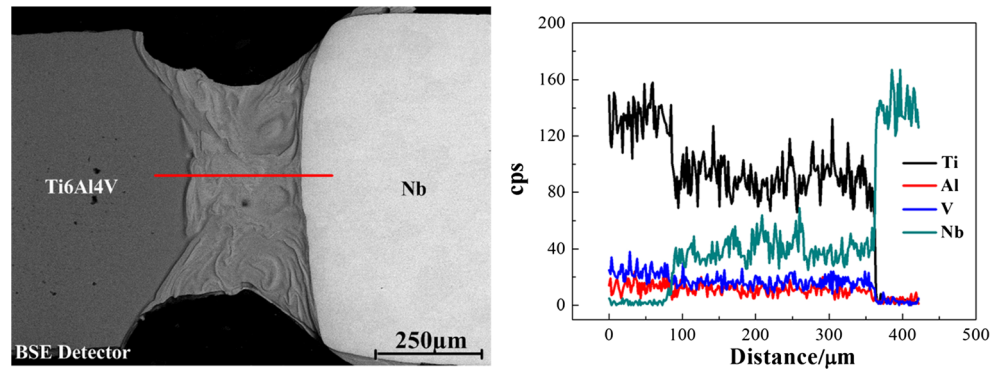

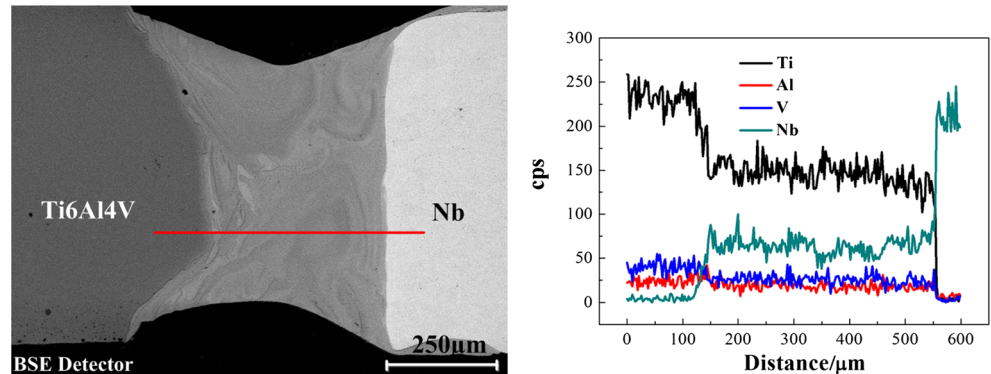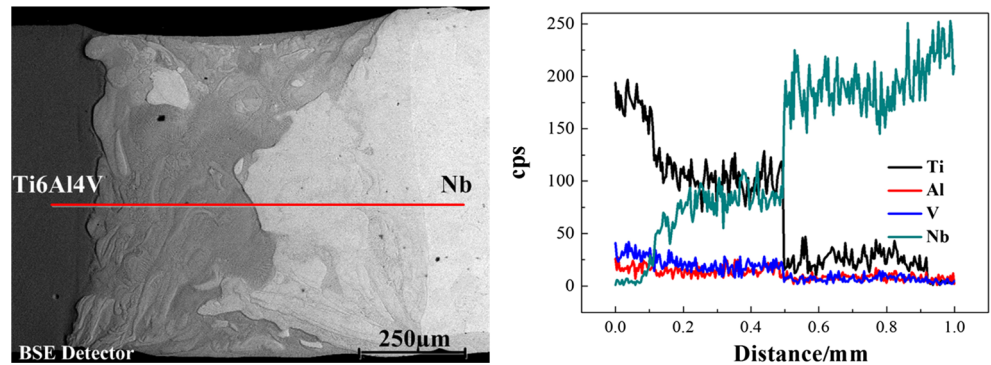**Fig. 13** SEM-EDS line-scanning results of the joints welded with $E = 45$ J mm^{-1}

**Fig. 14** SEM-EDS line-scanning results of the joints welded with $E = 67.5$ J mm^{-1}

along the scan line proceed from largest to smallest as $E = 67.5$, 22.5, and 45 J mm^{-1}. This result indicates that the heterogeneity of the elemental distribution is largest for the $E = 67.5$ J mm^{-1} welded joint, followed by the $E = 22.5$ J mm^{-1} and $E = 45$ J mm^{-1} welded joints. Overall, these results may be related to convective flow (i.e., the Marangoni effect), which is driven by temperature and surface tension gradients [24]. An increase in the laser energy resulted in an increased melt pool convection within the fusion zone [25]. Hence, the $E = 67.5$ J mm^{-1} welded joint exhibits the largest elemental distribution and microstructure heterogeneity.

Figure 15 shows the hardness distribution in the middle of the cross sections of the pulsed laser-

welded Ti6Al4V/Nb dissimilar joints with different heat inputs, where the average hardness of the FZ is shown at the center. For each heat input, the relationship among the microhardness values of the base metal, HAZ, and FZ of the Ti6Al4V/Nb dissimilar joint follows the trend: Ti6Al4V sheet > FZ > Nb sheet. The microhardness value of the Ti6Al4V sheet ranges from approximately 310 to 330 HV, whereas it ranges from approximately 80 to 100 HV for the Nb sheet. Although the melting point of pure niobium is relatively high, the hardness value of the Nb sheet after annealing processes is very low [18]. As shown in Fig. 15, the mean microhardness of the FZ decreases slightly with increasing heat input. This trend can be
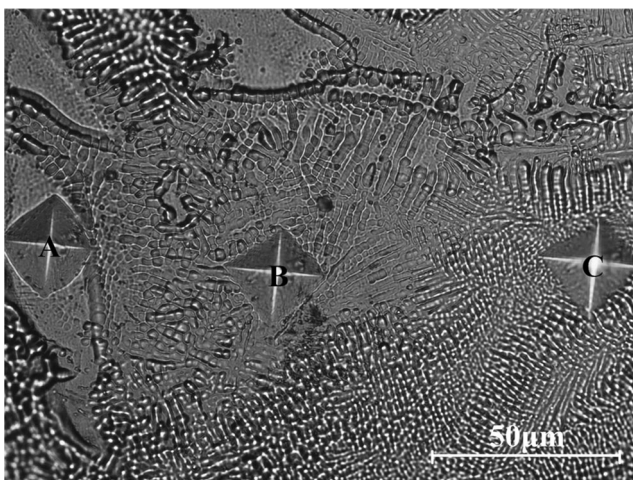
Fig. 15 Microhardness profiles of the weld cross-section for various heat inputs. **a** 22.5 J mm^{-1}, **b** 45 J mm^{-1}, and **c** 67.5 J mm^{-1}
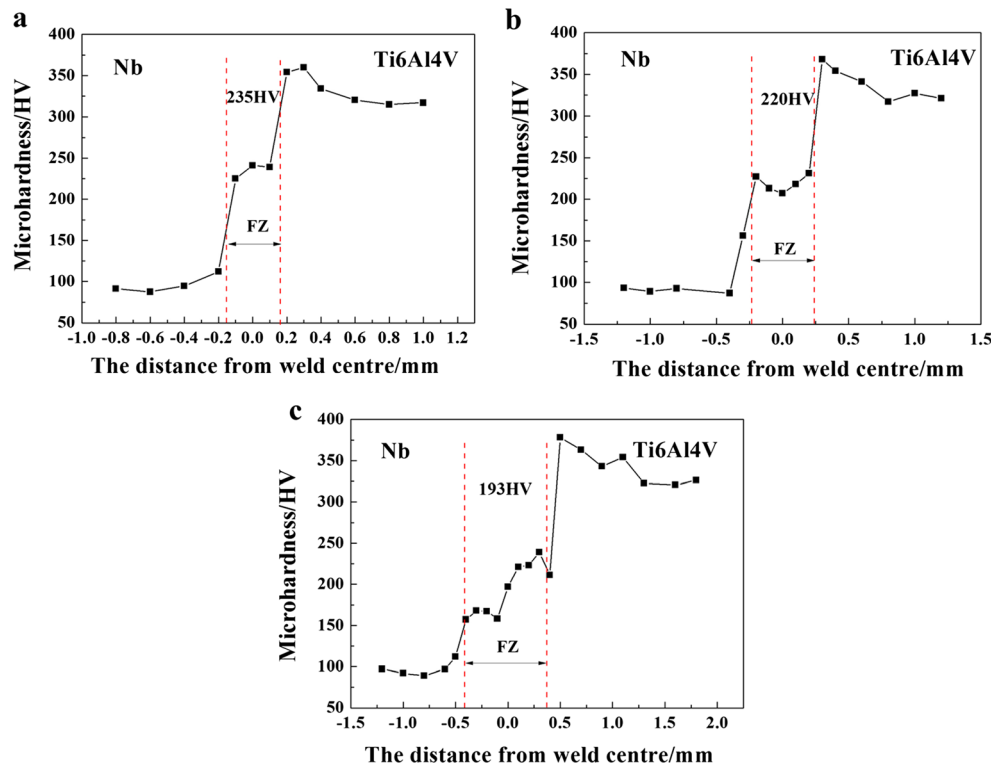
understood in terms of the increasing Nb content in the FZ for joints welded with high heat input. Fluctuations of the hardness value along the longitudinal direction are observed in the FZ for the Ti6Al4V/Nb dissimilar joint, which may be related to the distribution of its composition. Further, fluctuations of the hardness value along the longitudinal direction for 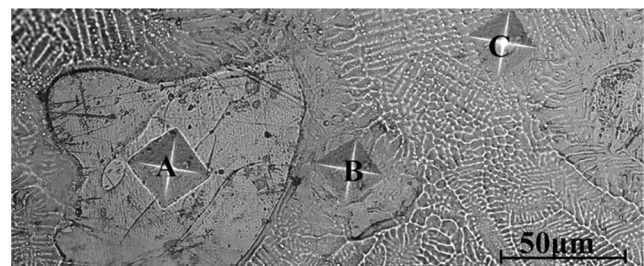the $E = 67.5$ J mm^{-1} welded joints are larger than the $E = 22.5$ J mm^{-1} and $E = 45$ J mm^{-1} welded joints, demonstrating that the $E = 67.5$ J mm^{-1} welded joint exhibits the highest mechanical heterogeneity.

Figures 16 and 17 show the microstructure and microhardness profiles in the island areas and dendritic zones for the $E = 45$ J mm^{-1} and $E = 67.5$ J mm^{-1} welded joints, respectively. For each heat input, the microhardness of the island area is lower than that of the dendritic zone. According the EDS analysis, the Nb content of the island area is greater than that of the dendritic zone, leading to the difference in their microstructures. Torkamany et al. have shown that zones containing higher amounts of Ti6Al4V have larger hardness

Microhardness	A	B	C
Value/HV	221	234	241

Fig. 16 Microstructure and microhardness profiles of the $E = 45$ J mm^{-1} welded joints

Microhardness	A	B	C
Value/HV	143	197	210

Fig. 17 Microstructure and microhardness profiles of the $E = 67.5$ J mm^{-1} welded joints
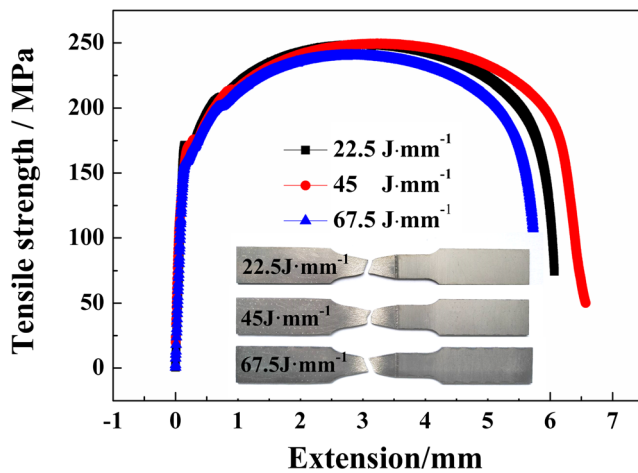
Fig. 18 Tensile curves of welded joints with different heat inputs

microscopic patterns were observed on the fracture surface of the welded joints, suggesting that the fracture occurs in a pure shear manner. These experimental results indicate that the strength of the FZ is higher than that of the Nb base metal, and the dissimilar joints possess relatively high tensile ductility.

4 Conclusions

1. As the heat input increases, the width of the heat-affected zone at the Ti6Al4V side increased significantly and underfill defects disappeared in the fusion zone (FZ).
2. No intermetallic compounds were formed in the FZ, but composition segregation occurred in the Ti6Al4V/Nb dissimilar joint.
3. The microstructure and mechanical heterogeneity in the FZ of the welded joints increased with increasing heat input.
4. The microhardness of the island area was lower than that of the dendritic zone for all dissimilar joints due to a higher Nb content in the island area.
5. The joints fractured at the Nb base metal side during the tensile tests, and the tensile strength of the welded joints was ~ 250 MPa.

values than those in regions with higher levels of Nb for pulsed laser-welded Ti6Al4V/Nb dissimilar metals [18].

The results of the tensile tests of the laser beam welded joints under different heat inputs are shown in Fig. 18. The dissimilar joints were broken from the Nb base metal side for the different heat inputs, and the tensile strength of the dissimilar joints was ~ 250 MPa. Figure 19 shows the fracture morphologies of the welded joints. As seen, ripple-shaped

Fig. 19 Morphology of the fracture surface of the tensile specimens
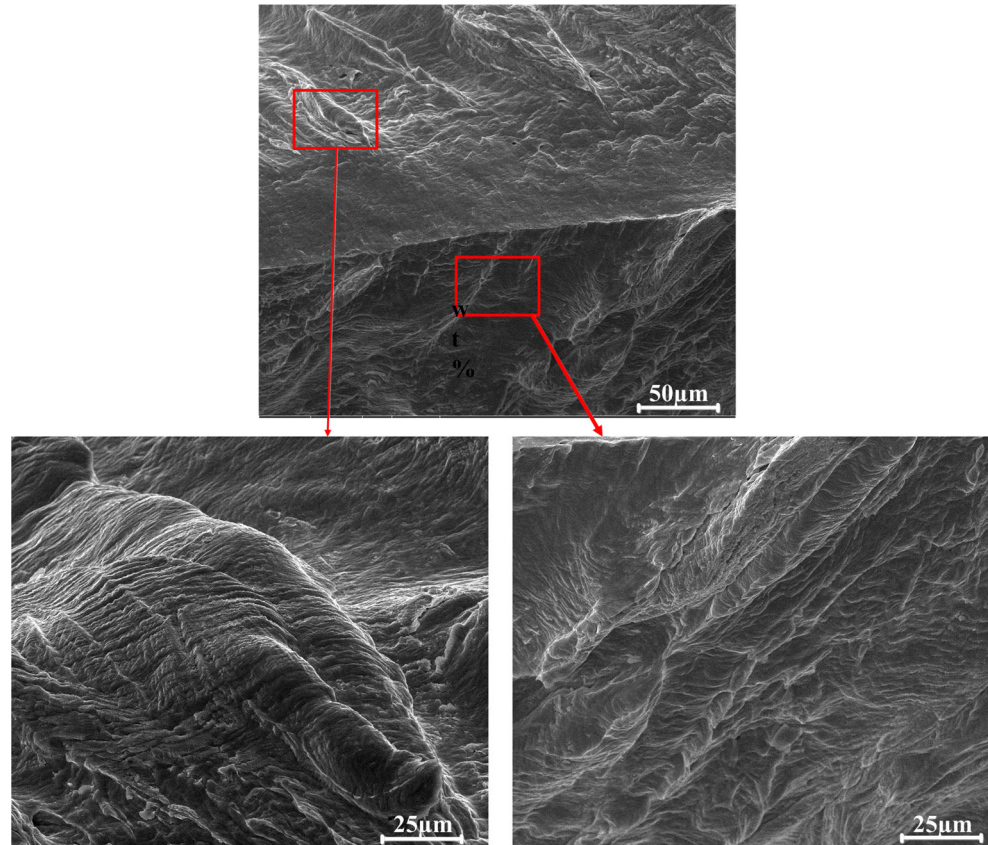
References

1. Gao XL, Zhang LJ, Liu J, Zhang JX (2014) Effects of weld cross-section profiles and microstructure on properties of pulsed Nd:YAG laser welding of Ti6Al4V sheet. Int J Adv Manuf Technol 72:895–903

2. Casalino G, Mortello M (2016) A FEM model to study the fiber laser welding of Ti6Al4V thin sheet. Int J Adv Manuf Technol 85:1339–1346

3. Grill R, Gnadenberger A (2006) Niobium as mint metal: production properties processing. Int J Refract Metal Hard Mater 24:275–282

4. Cooley LD, Burk D, Cooper C, Dhanaraj N, Foley M, Ford D (2011) Impact of forming, welding, and electropolishing on pitting and the surface finish of SRF cavity niobium. IEEE Trans Appl Supercond 21:2609–2614

5. Pouquet J, Miranda RM, Quintino L, Williams S (2012) Dissimilar laser welding of NiTi to stainless steel. Int J Adv Manuf Technol 61:205–212

6. Wang PF, Chen XZ, Pan QH, Madigan B, Long JQ (2016) Laser welding dissimilar materials of aluminum to steel: an overview. Int J Adv Manuf Technol 87:3081–3090

7. Chen YH, Mao YQ, Lu WW, He P (2017) Investigation of welding crack in micro laser welded NiTiNb shape memory alloy and Ti6Al4V alloy dissimilar metals joints. Opt Laser Eng 91:197–202

8. Miranda RM, Assunção E, Silva RJC, Oliveira JP, Quintino L (2015) Fiber laser welding of NiTi to Ti-6Al-4V. Int J Adv Manuf Technol 81:1533–1538

9. Satoh G, Yao LY, Qiu CA (2013) Strength and microstructure of laser fusion-welded Ti-SS dissimilar material pair. Int J Adv Manuf Technol 66:469–479

10. Sun M, Niknejad ST, Zhang G, Lee MK, Wu L, Zhou Y (2015) Microstructure and mechanical properties of resistance spot welded AZ31/AA5754 using a nickel interlayer. Mater Des 87:905–913

11. Penner P, Liu L, Gerlich A, Zhou Y (2013) Feasibility study of resistance spot welding of dissimilar Al/Mg combinations with Ni based interlayers. Sci Technol Weld Join 18:541–550

12. Kundu S, Chatterjee S (2010) Evolution of interface microstructure and mechanical properties of titanium/304 stainless steel diffusion bonded joint using Nb interlayer. ISIJ Int 50:1460–1465

13. Zhang Y, Sun DQ, Gu XY, Li HM (2016) A hybrid joint based on two kinds of bonding mechanisms for titanium alloy and stainless steel by pulsed laser welding. Mater Lett 185:152–155

14. Torkamany MJ, Hamedi MJ, Malek F, Sabbaghzadeh J (2006) The effect of process parameters on keyhole welding with a 400W Nd:YAG pulsed laser. J Phys D Appl Phys 39:4563–4567

15. Tzeng YF (2000) Process characterisation of pulsed Nd:YAG laser seam welding. Int J AdvManuf Technol 16:10–18

16. Chen HC, Bi GJ, Lee BY, Cheng CK (2016) Laser welding of CP Ti to stainless steel with different temporal pulse shapes. J Mater Process Tech 231:58–65

17. Oliveira JP, Panton B, Zeng Z, Andrei CM, Zhou Y, Miranda RM, Fernandes FMB (2016) Laser joining of NiTi to Ti6Al4V using a niobium interlayer. Acta Mater 105:9–15

18. Torkamany MJ, Ghaini FM, Poursalehi R (2014) Dissimilar pulsed Nd:YAG laser welding of pure niobium to Ti-6Al-4V. Mater Des 53:915–920

19. Torkamany MJ, Ghaini FM, Poursalehi R, Kaplan AFH (2016) Combination of laser keyhole and conduction welding: dissimilar laser welding of niobium and Ti-6Al-4V. Opt Laser Eng 79:9–15

20. Torkamany MJ, Ghaini FM, Poursalehi R (2016) An insight to the mechanism of weld penetration in dissimilar pulsed laser welding of niobium and Ti-6Al-4V. Opt Laser Eng 79:100–107

21. Oliveira JP, Zeng Z, Andrei C, Braz Fernandesc FM, Miranda RM, Ramirez AJ, Omori T, Zhou N (2017) Dissimilar laser welding of superelastic NiTi and CuAlMn shape memory alloys. Mater Des 128:166–175

22. ASM handbook volume 03. Alloy phase diagrams. ASM International; 1992. ISBN: 978-0-87170-381-1

23. Chen GL, Wang XT, Ni KQ, Hao SM, Cao JX, Ding JJ, Zhang X (1996) Investigation on the 1000, 1150 and 1400 °C isothermal section of the Ti-Al-Nb system. Intermetallics 4:13–22

24. Pang SY, Chen X, Zhou JX, Shao XY, Wang CM (2015) 3D transient multiphase model for keyhole, vapor plume, and weld pool dynamics in laser welding including the ambient pressure effect. Opt Laser Eng 74:47–58

25. Esfahani MRN, Coupland J, Marimuthu S (2015) Numerical simulation of alloy composition in dissimilar laser welding. J Mater Process Tech 224:135–142